

RING: Rabi oscillations induced by nonresonant geometric drive

Baksa Kolok^{1,2} and András Pályi^{1,2}

¹*Department of Theoretical Physics, Institute of Physics,
Budapest University of Technology and Economics, Műegyetem rkp. 3., H-1111 Budapest, Hungary*

²*HUN-REN-BME-BCE Quantum Technology Research Group,
Budapest University of Technology and Economics, Műegyetem rkp. 3., H-1111 Budapest, Hungary*

(Dated: February 13, 2026)

Coherent control of two-level quantum systems is typically achieved using resonant driving fields, forming the basis for qubit operations. Here, we report a mechanism for inducing complete Rabi oscillations in monochromatically driven two-level quantum systems, when the drive frequency is much larger than the Larmor frequency of the qubit. This effect—Rabi oscillations induced by nonresonant geometric drive (RING)—requires that the control field is elliptical, enclosing a nonzero area per cycle. We illustrate the effect with numerical simulations, and provide an analytical understanding via a simple effective Hamiltonian obtained from Floquet theory and perturbation theory. We show that RING enables coherent oscillations without relying on resonant energy exchange, allows for high-pass noise filtering, provides access to non-Abelian phases in finite magnetic fields. We detail a realization in electrically driven spin-orbit qubits and argue that the RING mechanism enables amplification of the Rabi frequency using the same gate voltage amplitudes at higher drive frequencies. Our results broaden the landscape of quantum control techniques, by highlighting a pathway to achieving coherent oscillations under off-resonant driving conditions.

I. INTRODUCTION

Coherent control of two-level quantum systems is typically achieved via Rabi oscillations induced by resonant driving. This mechanism enables high-fidelity qubit operations in various platforms, including superconducting circuits [1–6], trapped ions [7, 8], semiconductor spins [9–24] and cold atoms [25–27].

While resonant Rabi oscillations provide robust control, other strategies have emerged to address specific challenges. For instance, singlet-triplet qubits [28–33] and exchange-only qubits [34–37], where operations are driven by baseband pulses modifying the exchange interactions between spins. Another example is baseband control of hopping single spin qubits in semiconductor quantum dots [38–40], which alleviates the need for microwave control fields. A third example is holonomic quantum control, a scheme that provides partial tolerance against control errors [41–52], and in case of semiconductor quantum dot spin qubits alleviates the need for a magnetic field [53–55].

Here, we propose and theoretically demonstrate a control mechanism that enables complete Rabi oscillations without resonance; more precisely, by utilizing a monochromatic drive signal with a frequency exceeding the Larmor frequency. This effect, which we call Rabi oscillations induced by nonresonant geometric drive (RING), emerges when the qubit is driven by a circular or elliptic drive, which traces a finite-area loop in control space. The resulting oscillations broaden the quantum control toolbox by exploiting off-resonant dynamics.

The RING mechanism introduced here exhibits several distinctive features that set it apart from conventional qubit control schemes. It provides a route to demonstrating non-Abelian phases, in the context of spin-orbit coupled semiconductor spin qubits, in the presence of

a finite magnetic field, which is of fundamental interest and relevant for the development of holonomic quantum computation [53–55]. Moreover, by enabling full Rabi oscillations under far-detuned driving, it naturally allows for the integration of high-pass filtering to suppress low-frequency and resonant noise. Finally, the mechanism operates without relying on coherent energy exchange between the drive and the qubit, in contrast to standard resonant control protocols. At the same time, the RING drive can induce a Rabi frequency that is comparable to the Larmor frequency of the qubit, which opens the door to fast qubit manipulation for low-frequency qubits.

The rest of this paper is structured as follows. In Sec. II we present a minimal two-level model with elliptic drive, and demonstrate the RING mechanism numerically and analytically using Floquet and quasi-degenerate perturbation theory. In Sec. III we show that the non-Abelian Berry phase makes the RING drive possible in spin-orbit coupled semiconductor quantum dot devices. Section IV surveys experimental platforms and implementation challenges (pulse shaping, detuning robustness, and error mitigation). Finally, Section V summarizes our findings and outlines prospects for near-term demonstrations.

II. RING MECHANISM IN A DRIVEN TWO-LEVEL SYSTEM

In this section, we provide a minimal model for the RING mechanism. We consider a two-level system with a nonzero energy splitting (Larmor frequency $\omega_L/2\pi$), which is driven by two linearly polarized control fields that are orthogonal to each other, have the same driving frequency $\omega_d/2\pi$, and have a phase lag with respect to each other. This drive produces complete Rabi oscilla-

tions even if the drive frequency is much higher than the Larmor frequency.

To illustrate the effect, we first present numerical results for a rotating drive field. Then, we explain the observed dynamics using Floquet theory.

A. Numerical demonstration of the RING mechanism

The Hamiltonian of the two-level system with elliptically polarized drive reads as

$$H(t) = \frac{\hbar\omega_L}{2}\sigma_z + \frac{\hbar\Omega_{xz}}{2}\cos(\omega_d t + \phi_{xz})(\cos\vartheta\sigma_x + \sin\vartheta\sigma_z) + \frac{\hbar\Omega_y}{2}\cos(\omega_d t + \phi_y)\sigma_y, \quad (1)$$

where Ω_{xz}, Ω_y are driving amplitudes, ϕ_{xz}, ϕ_y are initial phases of the drive components, and ϑ is the angle between the static field and the normal vector of the driving field's plane, see Fig. 1(a).

Figure 1(b-c) shows the key result: complete Rabi oscillations, despite the drive frequency ω_d being far detuned from the Larmor frequency ω_L : in particular, Fig. 1(b) exhibits Rabi oscillations around $\omega_d/2\pi \approx 3$ GHz, while $\omega_L/2\pi = 25$ MHz. In this numerical demonstration, we set $\Omega_{xz} = \Omega_y$ and $\phi_{xz} = 0, \phi_y = -\pi/2$ for simplicity, and we set the initial state as the ground state of the static part of the Hamiltonian. In Fig. 1(b), the color scale shows the excited-state occupation probability p_e as the function of time and drive frequency. The excited state probability shows a chevron-like pattern similar to the case of a resonant drive; however, there are clear differences: (i) The pattern in Fig. 1(b) has no mirror symmetry axis at any value of the drive frequency, and (ii) the drive frequency corresponding to complete Rabi oscillations, marked by red dashed line, is not the same as the drive frequency corresponding to the lowest oscillation frequency.

To obtain Fig. 1(c), we simulated the time-dependent excited-state probability $p_e(t)$ for various values of the Larmor and drive frequencies, and plotted the maximum value of $p_e(t)$ as a function of the two frequencies. We observe the fingerprint of resonant Rabi oscillations in Fig. 1(c) as the white band at the bottom of the graph following the linear trend $\omega_d = \omega_L$. Besides that standard feature, another 'effective resonance' (full population inversion) occurs for driving frequencies highly above the Larmor frequency, following an $\omega_d \propto 1/\omega_L$ condition, also highlighted as the dashed red line. This is the fingerprint of the RING mechanism.

B. Analytical, perturbative description of the RING mechanism

We provide an analytical, perturbative description of the phenomena identified in the numerical simulations.

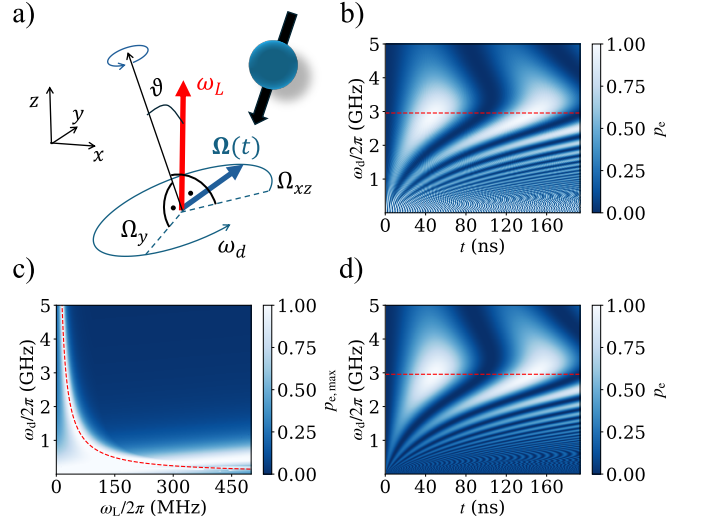


FIG. 1. Rabi oscillation induced by nonresonant geometric drive in a two-level system. (a) Schematics of the driving scheme inducing RING in a two-level system, represented by a spin (sphere with arrow). The static component of the Zeeman field (ω_L , red arrow) encloses a non-zero angle ϑ with the normal of the plane spanned by the drive fields ($\Omega(t)$, blue arrow). (b) Excited-state population p_e as a function of time and drive frequency. Initial state is the ground state $|\downarrow\rangle$ of the static part of the Hamiltonian (1), and the system is driven as specified by Eq. (1). Red dashed line: drive frequency corresponding to full Rabi oscillation. Data is obtained via numerical solution of the Schrödinger equation see Appendix A. Drive strengths: $\Omega_{xz}/2\pi = \Omega_y/2\pi = 400$ MHz. Tilt angle: $\vartheta = \pi/8$. Larmor frequency: $\omega_L/2\pi = 25$ MHz. Phases: $\phi_{xz} = 0$ and $\phi_y = -\pi/2$. (c) Maximum excited state population as a function of Larmor and drive frequencies, with parameters same as for panel (b). For each point, $p_e(t)$ was maximized in a time window of duration $T = 1000 \cdot 2\pi/\omega_d$. Besides the fundamental resonance at $\omega_d = \omega_L$ (and the fainter half-harmonic resonance at $\omega_d = \omega_L/2$), full population inversion occurs in the $\omega_d \gg \omega_L$ regime, with $\sim 1/\omega_L$ behavior. We have plotted the 'effective resonance' condition in Eq. (12) as a red dashed line. (d) Excited state population as a function of time and drive frequency, calculated analytically as in Eq. (10), with the same parameter values as panel (c). We marked the frequency of full Rabi oscillations with red dashed line, using Eq. (12).

By combining the Floquet formalism [56, 57] with quasi-degenerate perturbation theory [58–60], we explicitly derive an effective Hamiltonian in the high-frequency limit. While the dynamics of periodically driven systems in this regime have been studied extensively in the literature [61, 62], the specific configuration considered here has not been analyzed. We therefore present the full derivation to make the underlying mechanism explicit and enable a transparent interpretation of the results.

For a periodically driven two-level system, Floquet's theorem yields two solutions [56, 57] of the form $\Psi_\alpha(t) = e^{-i\epsilon_\alpha t/\hbar}\Phi_\alpha(t)$, where $\Phi_\alpha(t)$ is periodic with the drive period and $\alpha = \pm$ labels the Floquet states corresponding

to higher and lower quasienergy. We expand $\Phi_\alpha(t)$ in Fourier harmonics:

$$\Psi_\alpha(t) = e^{-i\epsilon_\alpha t/\hbar} \sum_{\sigma \in \{\uparrow, \downarrow\}} \sum_{n=-\infty}^{\infty} e^{in\omega_d t} c_{\alpha, \sigma n} |\sigma\rangle, \quad (2)$$

where $|\sigma\rangle$ denotes the eigenbasis of the undriven Hamiltonian.

Substituting the trial solution Eq. (2) to the time-dependent Schrödinger equation, one obtains an infinite-dimensional eigenvalue problem

$$\mathcal{F}\mathbf{c}_\alpha = \epsilon_\alpha \mathbf{c}_\alpha \quad (3)$$

for the Floquet matrix \mathcal{F} . The notation \mathbf{c}_α stands for an infinite vector of the coefficients in Eq. (2), ordered as $\mathbf{c}_\alpha = (\dots, c_{\alpha, \uparrow, -1}, c_{\alpha, \downarrow, -1}, c_{\alpha, \uparrow, 0}, \dots)^T$. For the Hamiltonian in Eq. (1), the Floquet matrix reads as:

$$\mathcal{F} = \begin{pmatrix} \ddots & \vdots & \vdots & \vdots & \vdots \\ \dots & H^{(0)} - \hbar\omega_d & H^{(-1)} & 0 & \dots \\ \dots & H^{(1)} & H^{(0)} & H^{(-1)} & \dots \\ \dots & 0 & H^{(1)} & H^{(0)} + \hbar\omega_d & \dots \\ \vdots & \vdots & \vdots & \vdots & \ddots \end{pmatrix}, \quad (4)$$

where each nonzero entry is a 2×2 block corresponding to the nonzero Fourier components of the Hamiltonian:

$$H^{(0)} = \frac{\hbar\omega_L}{2} \sigma_z, \quad (5a)$$

$$H^{(\pm 1)} = \frac{\hbar}{4} (e^{\pm i\phi_{xz}} \Omega_{xz} (\cos \vartheta \sigma_x + \sin \vartheta \sigma_z) + e^{\pm i\phi_y} \Omega_y \sigma_y). \quad (5b)$$

The eigenvalue equation for the Floquet matrix in Eq. (2) has infinitely many solutions, however, only two of the solutions are nonequivalent, e.g., those with quasienergy ϵ_α lying in the first ‘quasienergy Brillouin zone’: $-\hbar\omega_d/\pi < \epsilon_\alpha \leq \hbar\omega_d/\pi$ [56, 57].

The structure of the Floquet matrix is illustrated in Fig. 2, in the special case when $\Omega_{xz} = \Omega_y$ and $\phi_{xz} - \phi_y = \pi/2$, i.e., for circular drive. Each horizontal line represents an ‘unperturbed’ eigenvalue-eigenvector pair (or *Floquet level*) of the system, that is, an eigenvalue-eigenvector pair of the diagonal part of \mathcal{F} . These Floquet levels are organized in Fig. 2 into Fourier sectors labeled by $n = -1, 0, 1$. The harmonic drive introduces couplings between Floquet levels in neighboring sectors, shown as arrows in Fig. 2. The thickness of each arrow indicates the magnitude of the corresponding matrix element; for this figure, we assume $0 < \vartheta < \pi/2$. (Note that for $\vartheta > \pi/2$, the ordering of matrix-element magnitudes reverses, which makes the Rabi oscillation impossible.)

In the high-frequency drive limit, where $\omega_d \gg \omega_L, \Omega_{xz}, \Omega_y$, we use quasi-degenerate perturbation theory [58–60] to obtain an effective 2×2 Floquet matrix from \mathcal{F} , enabling to express the perturbed eigenvectors of

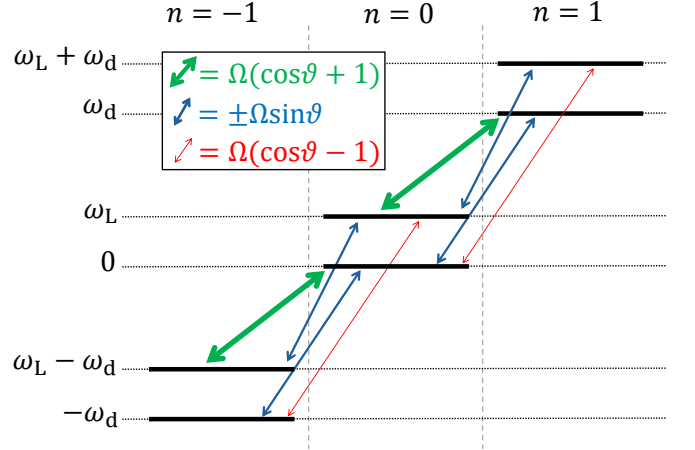


FIG. 2. Structure of the Floquet matrix. The figure shows three adjacent Fourier sectors ($n = -1, 0, 1$) of the Floquet ladder, each containing two unperturbed eigenstates split by the Larmor frequency ω_L . Arrows represent drive-induced couplings between states; their thickness reflects the magnitude of the matrix elements, which depends on the angle ϑ . For $0 < \vartheta < \pi/2$, this thickness hierarchy is preserved, resulting in a shift of energy levels that reduces the effective level splitting. For $\vartheta > \pi/2$, the hierarchy reverses. Within $0 < \vartheta < \pi/2$, this structure allows for a ‘effective resonance’ in the (Ω, ω_d) parameter space where Rabi oscillations are complete. Blue lines do not shift energy levels but enable coherent transitions; without them, Rabi oscillations vanish.

\mathcal{F} . This approach yields the following effective Floquet matrix, up to second order in ω_L and $\Omega_{x,y}$:

$$\mathcal{F}_{\text{eff}} = H^{(0)} + \frac{[H^{(1)}, H^{(-1)}]}{\hbar\omega_d} = \frac{\hbar}{2} (\Delta \sigma_z + \Omega_R \sigma_x). \quad (6)$$

Here, we introduced

$$\Delta = \omega_L - \frac{\Omega_{xz} \Omega_y \cos \vartheta \sin(\Delta\phi)}{2\omega_d}, \quad (7a)$$

$$\Omega_R = \frac{\Omega_{xz} \Omega_y \sin \vartheta \sin(\Delta\phi)}{2\omega_d}, \quad (7b)$$

and $\Delta\phi = \phi_{xz} - \phi_y$.

The effective Floquet matrix is the result of second order perturbation theory, which can be understood using Fig. 2. In the $0 < \vartheta < \pi/2$ regime, the level repulsion between $|0 \uparrow\rangle$ and $|1 \downarrow\rangle$ is stronger than the level repulsion between $|0 \uparrow\rangle$ and $|1 \downarrow\rangle$, while the level repulsions due to the states $|\pm 1 \uparrow\rangle$ cancel each other. This results in an overall decrease of the energy level. A similar argument shows that the level of $|0 \downarrow\rangle$ increases. Therefore, the gap between the states decreases, see Eq. (7a). In the meantime, the combination of the transverse and longitudinal coupling (green/red arrow and blue arrow) results in a second order matrix element between the $|0 \downarrow\rangle$ and $|0 \uparrow\rangle$ states, which results in Ω_R in Eq. (7b).

The time-evolved Floquet states $\Psi_\alpha(t)$ can be expressed via the diagonalization of the effective Floquet

matrix, and the unitary transformation corresponding to the Schrieffer–Wolff transformation e^S , which is used to perturbatively eliminate the off-diagonal blocks between the zeroth and the other Fourier sectors.

One obtains the leading order dynamics in the small parameters ω_L/ω_d , Ω_{xz}/ω_d , and Ω_y/ω_d when the Schrieffer–Wolff unitary e^S is approximated with the identity. In this approximation, $c_{\alpha,\sigma n}$ is only nonzero if $n = 0$, and the two nonzero coefficients form the eigenvectors of the effective Floquet matrix. The quasienergies ϵ_α are the corresponding eigenvalues of the effective Floquet matrix, thus the Floquet states, using Eq. (2), read as

$$\Psi_\alpha^{(0)}(t) = e^{-\frac{i}{\hbar}\epsilon_\alpha t} |f_\alpha\rangle = e^{-\frac{i}{\hbar}\mathcal{F}_{\text{eff}} t} |f_\alpha\rangle, \quad (8)$$

where $|f_\alpha\rangle$ are the eigenstates of the effective Floquet matrix for $\alpha = \pm$. The time-evolution operator reads as

$$U^{(0)}(t) = \sum_{\alpha \in \{+,-\}} \left| \Psi_\alpha^{(0)}(t) \right\rangle \left\langle \Psi_\alpha^{(0)}(0) \right| = e^{-\frac{i}{\hbar}\mathcal{F}_{\text{eff}} t}, \quad (9)$$

where we used Eq. (8) and the fact that eigenvectors of the effective Floquet matrix $|f_\alpha\rangle$ form a basis. Finally, the excited-state population, when the system is initialized in $|\downarrow\rangle$, reads as

$$\begin{aligned} p_e(t) &= \left| \langle \uparrow | e^{-\frac{i}{\hbar}\mathcal{F}_{\text{eff}} t} |\downarrow \rangle \right|^2 \\ &= \frac{\Omega_R^2}{\Omega_R^2 + \Delta^2} \sin^2 \left(\frac{\sqrt{\Omega_R^2 + \Delta^2}}{2} t \right), \end{aligned} \quad (10)$$

with the parameters defined in Eqs. (7).

The “effective resonance” condition, when the system performs complete Rabi oscillations, is fulfilled when $\Delta = 0$, i.e. from Eq. (7a) it follows that

$$\omega_L = \frac{\Omega_{xz}\Omega_y \cos \vartheta \sin(\Delta\phi)}{2\omega_d}. \quad (11)$$

Note that at the effective resonance, it holds that $\omega_L \ll \Omega_{xz}, \Omega_y$. We call the drive frequency satisfying the effective resonance condition in Eq. (11) as the RING frequency and denote it as

$$\omega_{\text{RING}} = \frac{\Omega_{xz}\Omega_y \cos \vartheta \sin(\Delta\phi)}{2\omega_L}. \quad (12)$$

Another interesting consequence of Eq. (11), is that the Rabi frequency is proportional to the Larmor frequency and not to the driving field amplitude:

$$\Omega_R = \omega_L \tan \vartheta, \quad (13)$$

where we used Eqs. (7b) and (11). Practically this means that, unlike in the resonant drive case, by increasing the drive amplitude one cannot increase the Rabi frequency, it just detunes the RING frequency, see Eq. (12). The Rabi frequency, for a given Larmor frequency and angle

ϑ , is fixed as long as the effective resonance condition in Eq. (11) is fulfilled.

In Fig. 1(d), we have plotted the induced dynamics, in terms of the excited-state probability p_e , using Eqs. (10) and (7). The approximate analytical solution agrees with the numerical results in Fig. 1(b) up to fine structure.

The fine structure of the numerical dynamics can be estimated from the first order approximation of the unitary transformation corresponding to the Schrieffer–Wolff transformation: $e^S = I + S$. The S matrix, up to first order, reads as

$$S = \begin{pmatrix} \ddots & \vdots & \vdots & \vdots & \vdots \\ \cdots & 0 & \frac{H^{(-1)}}{\hbar\omega} & 0 & \cdots \\ \cdots & -\frac{H^{(1)}}{\hbar\omega} & 0 & \frac{H^{(-1)}}{\hbar\omega} & \cdots \\ \cdots & 0 & -\frac{H^{(1)}}{\hbar\omega} & 0 & \cdots \\ \vdots & \vdots & \vdots & \vdots & \ddots \end{pmatrix}, \quad (14)$$

where all the blocks indicated by dots are zeros. One obtains the \mathbf{c}_α vector by acting with $I + S$ on the zeroth order vector which has nonzero elements in the zeroth Fourier sector. The resulting vector has 4 additional nonzero elements in the $n = \pm 1$ Fourier sectors, these two-element blocks read as

$$\begin{pmatrix} c_{\alpha\uparrow,\pm 1} \\ c_{\alpha\downarrow,\pm 1} \end{pmatrix} = \mp \frac{H^{(\pm 1)}}{\hbar\omega} \begin{pmatrix} c_{\alpha\uparrow,0} \\ c_{\alpha\downarrow,0} \end{pmatrix}. \quad (15)$$

Therefore the Floquet states, reconstructed from Eq. (2) using Eqs. (8) and (15), read as

$$|\Psi_\alpha(t)\rangle = (I + \tilde{S}(t)) |\Psi_\alpha^{(0)}(t)\rangle, \quad (16)$$

where

$$\tilde{S}(t) = \frac{e^{-i\omega_d t} H^{(-1)} - e^{i\omega_d t} H^{(1)}}{\hbar\omega_d}. \quad (17)$$

The time-evolution operator, expressed with the Floquet states and using Eqs. (9) and (16) and neglecting second order terms, reads as

$$\begin{aligned} U(t) &= \sum_{\alpha \in \{+,-\}} |\Psi_\alpha(t)\rangle \langle \Psi_\alpha(0)| \\ &= e^{-\frac{i}{\hbar}\mathcal{F}_{\text{eff}} t} + \tilde{S}(t) e^{-\frac{i}{\hbar}\mathcal{F}_{\text{eff}} t} - e^{-\frac{i}{\hbar}\mathcal{F}_{\text{eff}} t} \tilde{S}(0). \end{aligned} \quad (18)$$

We express the correction to the excited-state population at the effective resonance ($\Delta = 0$) using Eq. (18) up to first order in the small parameters ω_L/ω_d , Ω_{xz}/ω_d , and Ω_y/ω_d . This yields

$$\begin{aligned} \delta p_e(t) &= \frac{\Omega_{xz} \cos \vartheta}{2\omega_d} \sin \Omega_R t [\sin(\omega_d t - \phi_{xz}) + \sin(\phi_{xz})] \\ &= \frac{\omega_L}{2\Omega_y \sin \Delta\phi} \sin \Omega_R t [\sin(\omega_d t - \phi_{xz}) + \sin(\phi_{xz})]. \end{aligned} \quad (19)$$

The quickly oscillating correction, in the context of resonant drive, is called the Bloch–Siegert oscillation [63], therefore we use the same terminology for the corrections of the RING as well.

The broadening of the “effective resonance” in Fig. 1(c) is captured by the drive frequency range for a fixed Larmor frequency, where the maximum excited state population reaches at least 1/2. The half population inversion for a given Larmor frequency yields the condition $\Delta = \Omega_R$ from Eq. (10) in leading order. The drive frequency detuning corresponding to this condition, from Eqs. (7) and (12), reads as

$$\Delta\omega^\pm = \pm\omega_{\text{RING}} \tan\vartheta. \quad (20)$$

The geometric nature underlying RING drive is quantified by the factor $\Omega_{xz}\Omega_y \sin \Delta\phi$ in Eqs. (7), which represents the signed area swept by the driving field’s elliptical path during each cycle. This geometric feature is central to the emergence of asymmetric coupling between Fourier sectors, see Fig. (2).

III. RING DRIVE OF SPIN-ORBIT COUPLED LOSS-DIVINCENZO QUBITS

We now consider the RING mechanism in a spin-orbit coupled quantum dot occupied by a single particle with spin- $\frac{1}{2}$, where qubit control is achieved via electric fields, see Fig. 3(a). For simplicity, we study an isotropic, harmonic confinement with Rashba spin-orbit coupling, driven by a circularly polarized electric field. The phenomenon exists in case of a more general confinement potential and spin-orbit interaction as well; we leave the description of such generalized cases for future work.

The Hamiltonian of the real-space effective-mass model of an isotropic quantum dot driven by circularly polarized electric field reads as:

$$H = H_0 + H_{\text{so}} + V_d(t) + \frac{1}{2}\hbar\tilde{\omega}_L \cdot \boldsymbol{\sigma}, \quad (21a)$$

$$H_0 = \frac{p^2}{2m} + \frac{1}{2}m\omega_0^2(x^2 + y^2), \quad (21b)$$

$$H_{\text{so}} = \alpha(p_x\sigma_y - p_y\sigma_x), \quad (21c)$$

$$V_d(t) = e\mathbf{r} \cdot \mathbf{E}_d(t), \quad (21d)$$

where $\hbar\tilde{\omega}$ is the Zeeman field in energy units coupled to the spin degree of freedom, m is the effective mass of the electron, ω_0 is the strength of the harmonic confinement, α is the strength of the spin-orbit interaction, e is the elementary charge, and $\mathbf{E}_d(t)$ is a rotating electric field:

$$\mathbf{E}_d(t) = E_0 \begin{pmatrix} \cos\omega_d t \\ \sin\omega_d t \\ 0 \end{pmatrix}. \quad (22)$$

To avoid a sudden quench at $t = 0$, we assume that for $t < 0$ a static electric field is already switched on in the x direction, i.e. $\mathbf{E}_d(t < 0) = \mathbf{E}_d(0)$.

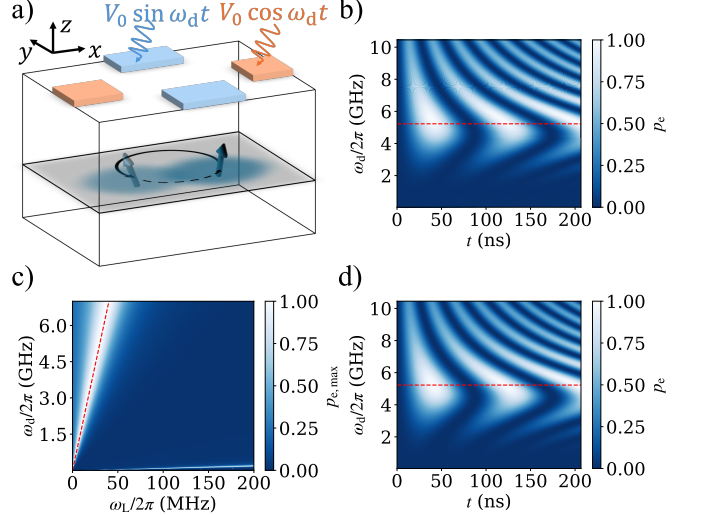


FIG. 3. Numerical and theoretical demonstration of the RING mechanism in electrically driven spin qubits. (a) Schematic figure of the electrically driven quantum dot using two electrodes. (b) Excited state population as a function of time and drive frequency, from numerical solution of Eq. (21). The parameters are set to the values: $E_0 = 4.4$ V/mm, $\vartheta = \pi/8$, $\alpha = 6500 \frac{\text{m}}{\text{s}}$, $\omega_0/2\pi = 140$ GHz, $\omega_L/2\pi = 30$ MHz, $m = 0.05m_e$, where m_e is the free electron mass. Red dashed line: drive frequency corresponding to full Rabi oscillation. (c) Maximum excited state population as a function of Larmor and drive frequencies, with the same parameters as in panel (b). Besides the resonant line, full population inversion occurs in the $\omega_d \gg \omega_L$ regime. We have plotted the ‘effective resonance’ condition in Eq. (45) with red dashed line. (d) Excited state population as a function of time and drive frequency, calculated analytically, with the same parameter values as panel (b). We marked the frequency of full Rabi oscillations with red dashed line using Eq. (45).

Our goal is to describe the time evolution of an initial state that is in the orbital ground-state subspace, i.e., a superposition of the two lowest-energy eigenstates of $H(t = 0)$. Furthermore, we describe the dynamics for an intermediate driving frequency, i.e., when the driving frequency is much greater than the Larmor frequency, but in the limit when

$$\omega_d e E_0 \ell_d \ll \hbar\omega_0^2, \quad (23)$$

where $\ell_d = \sqrt{\hbar/m\omega_0}$ is the confinement length of the quantum dot. In this case, the probability of the system leaving the orbital ground state is negligible, but significant dynamics is induced within the two lowest-energy instantaneous energy eigenstates of the time-dependent Hamiltonian.

A natural strategy to describe the dynamics in this case is to compute the time dependence of the instantaneous eigenstates of the time-dependent Hamiltonian, transform the time-dependent Schrodinger equation into that time-dependent instantaneous eigenbasis, and truncate the transformed Hamiltonian matrix to the two-dimensional ground-state subspace. Instead of using this

approach directly, we convert it to analytically tractable procedure by a slight modification and a further approximative step.

(1) *Spin-orbit dressed eigenstates.* We perturbatively compute the energy eigenstates of $H_0 + H_{\text{so}}$, taking the spin-orbit interaction term as the perturbation.

(2) *Spatial translation.* We calculate the instantaneous eigenstates of $H_0 + H_{\text{so}} + V_d(t)$ via the spatial translation of the wavefunctions calculated in the previous step.

(3) *Instantaneous eigenstate frame and truncation.* We transform the time-dependent Schrödinger equation, incorporating the Zeeman term, into the frame defined by these instantaneous, spin-orbit-dressed eigenstates, and truncate the transformed Hamiltonian to the two-dimensional ground-state subspace.

(4) *Floquet analysis.* Step (3) yields a 2×2 time-dependent effective Hamiltonian. We analyze the induced dynamics using Floquet theory.

Step (1): Spin-orbit dressed eigenstates. As the first step of the derivation of the effective Hamiltonian we calculate the spin-orbit dressed ground-state Kramers pair of $H_0 + H_{\text{so}}$ using perturbation theory. In the absence of spin-orbit interaction, the ground-state doublet is simply the product of the spin doublet and the ground state of the harmonic confinement:

$$|\psi_\sigma\rangle = \frac{1}{\ell_d \sqrt{\pi}} e^{-\frac{r^2}{2\ell_d^2}} |\sigma\rangle, \quad (24)$$

where $\sigma \in \{\uparrow, \downarrow\}$ labels the eigenstates of σ_z and $\ell_d = \sqrt{\frac{\hbar}{m\omega_0}}$. We apply third-order Schrieffer–Wolff transformation to find the lowest energy subspace of the spin-orbit coupled harmonic oscillator perturbatively [58–60]. The anti-hermitian generator of the Schrieffer–Wolff transformation reads as

$$S = S^{(1)} + S^{(2)} + S^{(3)}, \quad (25a)$$

$$S^{(1)} = \frac{i\ell_d}{\sqrt{2}\ell_{\text{so}}} (\sigma_x a_y^\dagger - \sigma_y a_x^\dagger) P_0 - \text{h.c.}, \quad (25b)$$

$$S^{(2)} = -\frac{\ell_d^2}{4\ell_{\text{so}}^2} (a_x^{\dagger 2} + a_y^{\dagger 2}) P_0 - \text{h.c.}, \quad (25c)$$

$$S^{(3)} = -\frac{i\ell_d^3}{12\sqrt{2}\ell_{\text{so}}^3} \left[\sigma_x (2a_y^\dagger + a_y^{\dagger 3} + a_x^{\dagger 2} a_y^\dagger) - \sigma_y (2a_x^\dagger + a_x^{\dagger 3} + a_y^{\dagger 2} a_x^\dagger) \right] P_0 - \text{h.c.}, \quad (25d)$$

where $\ell_{\text{so}} = \frac{\hbar}{m\alpha}$, $P_0 = |\psi_\uparrow\rangle\langle\psi_\uparrow| + |\psi_\downarrow\rangle\langle\psi_\downarrow|$ is the projector

to the lowest energy subspace of the 2D isotropic harmonic oscillator without spin-orbit interaction, and a_x^\dagger and a_y^\dagger are creation operators:

$$a_x^\dagger = \frac{1}{\sqrt{2}\ell_d} \left(x - \frac{i}{m\omega_0} p_x \right), \quad (26a)$$

$$a_y^\dagger = \frac{1}{\sqrt{2}\ell_d} \left(y - \frac{i}{m\omega_0} p_y \right). \quad (26b)$$

The generators are obtained such that

$$\tilde{H} = e^{-S} (H_0 + H_{\text{so}}) e^S \quad (27)$$

is block-diagonal up to third order, i.e. the two-fold degenerate ground state of \tilde{H} is decoupled from all other states. The approximative ground-state Kramers pair of $H_0 + H_{\text{so}}$ then reads as

$$|\Psi_\sigma\rangle = e^S |\psi_\sigma\rangle. \quad (28)$$

Step (2): Spatial translation. The next step is to switch on the drive, which essentially moves the center of the harmonic oscillator on the trajectory:

$$\mathbf{R}_d(t) = -\frac{e\mathbf{E}_d(t)}{m\omega_0^2}, \quad (29)$$

up to a time-dependent constant term in the Hamiltonian. Therefore, to find the instantaneous lowest energy subspace of $H_0 + H_{\text{so}} + V_d(t)$, we spatially translate the wavefunction in Eq. (28). The result is a parameter dependent Schrieffer–Wolff transformation $S_{\mathbf{R}_d}$, where the parameter \mathbf{R}_d only appears in the creation operators

$$a_x^\dagger(\mathbf{R}_d) = \frac{1}{\sqrt{2}\ell_d} \left(x - R_{d,x} - \frac{i}{m\omega_0} p_x \right), \quad (30a)$$

$$a_y^\dagger(\mathbf{R}_d) = \frac{1}{\sqrt{2}\ell_d} \left(y - R_{d,y} - \frac{i}{m\omega_0} p_y \right), \quad (30b)$$

and the projector $P_0(\mathbf{R}_d)$, which projects to the ground state of the shifted harmonic oscillator:

$$|\psi_\sigma(\mathbf{R}_d)\rangle = \frac{1}{\ell_d \sqrt{\pi}} e^{-\frac{(r-\mathbf{R}_d)^2}{2\ell_d^2}} |\sigma\rangle. \quad (31)$$

The instantaneous ground state doublet of $H_0 + H_{\text{so}} + V_d(t)$, up to third order are obtained using Eqs. (25), (30) and (31). It reads as

$$|\Psi_\sigma(\mathbf{R}_d)\rangle = e^{S_{\mathbf{R}_d}} |\psi_\sigma(\mathbf{R}_d)\rangle \approx \left[\left(1 - \frac{\ell_d^2}{2\ell_{\text{so}}^2} \right) I + \frac{i\ell_d}{\sqrt{2}\ell_{\text{so}}} \left(1 - \frac{\ell_d^2}{3\ell_{\text{so}}^2} \right) (\sigma_x a_y^\dagger(\mathbf{R}_d) - \sigma_y a_x^\dagger(\mathbf{R}_d)) - \frac{\ell_d^2}{4\ell_{\text{so}}^2} (a_x^{\dagger 2}(\mathbf{R}_d) + a_y^{\dagger 2}(\mathbf{R}_d)) \right. \\ \left. - \frac{i\ell_d^3}{12\sqrt{2}\ell_{\text{so}}^3} \left(\sigma_x (a_y^{\dagger 3}(\mathbf{R}_d) + a_x^{\dagger 2}(\mathbf{R}_d) a_y^\dagger(\mathbf{R}_d)) - \sigma_y (a_x^{\dagger 3}(\mathbf{R}_d) + a_x^\dagger(\mathbf{R}_d) a_y^{\dagger 2}(\mathbf{R}_d)) \right) \right] |\psi_\sigma(\mathbf{R}_d)\rangle. \quad (32)$$

Step (3): Instantaneous eigenstate frame and truncation. The final step to obtain the effective Hamiltonian is to

transform the full Hamiltonian to the instantaneous eigenbasis of $H_0 + H_{\text{so}} + V_{\text{d}}(t)$ and truncate the Hamiltonian to the two-dimensional ground-state subspace. The result is a 2×2 effective Hamiltonian, that can be separated to a time-independent and a time-dependent part:

$$H_{\text{eff}} = \frac{\hbar}{2}(\boldsymbol{\omega}_{\text{L}} + \boldsymbol{\Omega}_{\text{d}}(t)) \cdot \boldsymbol{\sigma}. \quad (33)$$

The static term is the renormalized Zeeman term:

$$\boldsymbol{\omega}_{\text{L}} \cdot \boldsymbol{\sigma} := P(\mathbf{R}_{\text{d}})\tilde{\boldsymbol{\omega}}_{\text{L}} \cdot \boldsymbol{\sigma}P(\mathbf{R}_{\text{d}}) = \mathbf{Z}\tilde{\boldsymbol{\omega}}_{\text{L}} \cdot \boldsymbol{\sigma}, \quad (34)$$

where

$$P(\mathbf{R}_{\text{d}}) = \sum_{\sigma=\uparrow,\downarrow} |\Psi_{\sigma}(\mathbf{R}_{\text{d}})\rangle\langle\Psi_{\sigma}(\mathbf{R}_{\text{d}})| \quad (35a)$$

is the projection to the instantaneous ground-state subspace, and

$$\mathbf{Z} = \begin{pmatrix} 1 - \frac{\ell_{\text{d}}^2}{\ell_{\text{so}}^2} & 0 & 0 \\ 0 & 1 - \frac{\ell_{\text{d}}^2}{\ell_{\text{so}}^2} & 0 \\ 0 & 0 & 1 - \frac{2\ell_{\text{d}}^2}{\ell_{\text{so}}^2} \end{pmatrix} \quad (36a)$$

is the renormalization of the Zeeman term up to third order in $\ell_{\text{d}}/\ell_{\text{so}}$ (the third order correction is zero).

The second term is identified as the non-Abelian Berry connection [64, 65], which arises from the time dependence of the eigenstates through the parameters $\mathbf{R}_{\text{d}}(t)$ and reads as

$$\boldsymbol{\Omega}_{\text{d}}(t) \cdot \boldsymbol{\sigma} := -2i \sum_{\sigma,\sigma'=\uparrow,\downarrow} |\Psi_{\sigma}(\mathbf{R}_{\text{d}})\rangle\langle\Psi_{\sigma'}(\mathbf{R}_{\text{d}})| \left\langle \Psi_{\sigma}(\mathbf{R}_{\text{d}}) \left| \dot{\mathbf{R}}_{\text{d}} \nabla_{\mathbf{R}_{\text{d}}} \Psi'_{\sigma}(\mathbf{R}_{\text{d}}) \right. \right\rangle. \quad (37)$$

To calculate the vector $\boldsymbol{\Omega}_{\text{d}}(t)$ one needs to evaluate the derivative of the basis vectors:

$$\begin{aligned} |\partial_{R_{\text{d},x}} \Psi_{\sigma}\rangle &= \left[\frac{1}{\sqrt{2}\ell_{\text{d}}} a_x^{\dagger} + \frac{i}{2\ell_{\text{so}}} \left(1 - \frac{\ell_{\text{d}}^2}{3\ell_{\text{so}}^2} \right) [\sigma_y(1 - a_x^{\dagger 2}) + \sigma_x a_x^{\dagger} a_y^{\dagger}] - \frac{\ell_{\text{d}}}{4\sqrt{2}\ell_{\text{so}}^2} a_x^{\dagger} (a_x^{\dagger 2} + a_y^{\dagger 2}) \right. \\ &\quad \left. - \frac{i\ell_{\text{d}}^2}{24\ell_{\text{so}}^3} \left(\sigma_x a_x^{\dagger} [a_y^{\dagger 3} + a_x^{\dagger 2} a_y^{\dagger} - 2a_y^{\dagger}] - \sigma_y [a_x^{\dagger 4} + a_x^{\dagger 2} a_y^{\dagger 2} - 3a_x^{\dagger 2} - a_y^{\dagger 2}] \right) \right] |\psi_{\sigma}\rangle, \end{aligned} \quad (38)$$

where, for brevity, we have omitted the \mathbf{R}_{d} dependence, and used the identities

$$\partial_{R_{\text{d},x}} a_x^{\dagger}(\mathbf{R}_{\text{d}}) = -\frac{1}{\sqrt{2}\ell_{\text{d}}}, \quad (39a)$$

$$\begin{aligned} \partial_{R_{\text{d},x}} |\psi_{\sigma}(\mathbf{R}_{\text{d}})\rangle &= \frac{\mathbf{r} - \mathbf{R}_{\text{d}}}{\ell_{\text{d}}^2} |\psi_{\sigma}(\mathbf{R}_{\text{d}})\rangle \\ &= \frac{1}{\sqrt{2}\ell_{\text{d}}} a_x^{\dagger}(\mathbf{R}_{\text{d}}) |\psi_{\sigma}(\mathbf{R}_{\text{d}})\rangle. \end{aligned} \quad (39b)$$

Finally, multiplying with $\langle\psi_{\sigma}(\mathbf{R}_{\text{d}})|$ from the left results in

$$\langle\Psi_{\sigma}(\mathbf{R}_{\text{d}}) | \partial_{R_{\text{d},x}} \Psi_{\sigma'}(\mathbf{R}_{\text{d}}) \rangle = \frac{i}{\ell_{\text{so}}} \left(1 - \frac{\ell_{\text{d}}^2}{3\ell_{\text{so}}^2} \right) \langle\sigma| \sigma_y | \sigma' \rangle, \quad (40)$$

up to third order in spin-orbit interaction. Similarly, the

other derivative reads as

$$\langle\Psi_{\sigma}(\mathbf{R}_{\text{d}}) | \partial_{R_{\text{d},y}} \Psi_{\sigma'}(\mathbf{R}_{\text{d}}) \rangle = -\frac{i}{\ell_{\text{so}}} \left(1 - \frac{\ell_{\text{d}}^2}{3\ell_{\text{so}}^2} \right) \langle\sigma| \sigma_x | \sigma' \rangle. \quad (41)$$

The $\boldsymbol{\Omega}_{\text{d}}(t)$ vector, expressed from Eq. (37) using Eqs. (29), (40) and (41), reads as

$$\boldsymbol{\Omega}_{\text{d}}(t) = \frac{2\omega_{\text{d}}\tilde{\alpha}eE_0}{\hbar\omega_0^2} \begin{pmatrix} \cos\omega_{\text{d}}t \\ \sin\omega_{\text{d}}t \\ 0 \end{pmatrix}, \quad (42)$$

where $\tilde{\alpha} = \alpha(1 - \ell_{\text{d}}^2/3\ell_{\text{so}}^2)$.

Step (4): Floquet analysis. The resulting time-dependent two-level Hamiltonian is equivalent to the model in Sec. II, therefore the same Floquet analysis can be applied. This results in the effective Hamiltonian in

Eq. (6), with parameters:

$$\Delta = \omega_L - \frac{2\omega_d e^2 E_0^2 \tilde{\alpha}^2 \cos \vartheta}{\hbar^2 \omega_0^4}, \quad (43a)$$

$$\Omega_R = \frac{2\omega_d e^2 E_0^2 \tilde{\alpha}^2 \sin \vartheta}{\hbar^2 \omega_0^4}, \quad (43b)$$

where ϑ is the angle between ω_L and the z axis. The system performs full Rabi oscillation at the ‘effective resonance’, when $\Delta = 0$ in Eq. (43a). This condition is fulfilled when

$$\omega_L = \frac{2\omega_d e^2 E_0^2 \tilde{\alpha}^2 \cos \vartheta}{\hbar^2 \omega_0^4}. \quad (44)$$

The drive frequency for full Rabi oscillations, called the RING frequency, is expressed from Eq. (44) as

$$\omega_{\text{RING}} = \frac{\hbar^2 \omega_0^4}{2e^2 E_0^2 \tilde{\alpha}^2 \cos \vartheta} \omega_L. \quad (45)$$

The Rabi frequency at the ‘effective resonance’ is the same as in Eq. (13), it only depends on the Larmor frequency and the direction of the renormalized Zeeman field ω_L .

We analyzed the dynamics using three complementary methods: (i) full numerical simulation of the real-space Hamiltonian in Eq. (21) relying on tight-binding discretization, (ii) a hybrid numerical-analytical solution based on the effective Floquet matrix in Eq. (6) with parameters from Eqs. (43), and (iii) an analytical solution of the effective Floquet dynamics from Eq. (6).

Figure 3(b) shows results from method (i). Similarly to the two-level minimal model presented in the previous section, a chevron-like pattern emerges, with the two differences with respect to the case of resonant drive: the pattern has no symmetry axis at any drive frequency value, and the complete Rabi oscillation appears at a drive frequency different from the drive frequency of the slowest Rabi oscillation. Figure 3(c) is obtained with method (ii), and only the maximum value of the excited state probability is plotted. In addition to the conventional resonant response, full population inversion appears at high drive frequency, in agreement with our analysis. For comparison, Fig. 3(d) shows the approximate analytical result from (iii). The plots agree with the numerical solutions in panel (b) up to fine structure, which is the signature of the Bloch–Siegert oscillations, neglected in the analytical solution.

We have written the details of the numerical simulations in Appendix A and made the code available in [66].

The drive frequency of half population inversion is obtained from the condition $\Delta = \pm \Omega$, which results in

$$\Delta \omega^{\pm} = \frac{\pm \sin \vartheta}{\cos \vartheta \pm \sin \vartheta} \omega_{\text{RING}}, \quad (46)$$

where ω_{RING} is the driving frequency at the ‘effective resonance’ defined in Eq. (45).

Interestingly, the amplitude of the Bloch–Siegert oscillation does not depend on the drive frequency at the effective resonance, because the effective driving field Ω_d is proportional to ω_d . Therefore, from Eqs. (19) and (42), the amplitude reads as

$$A_{\text{BS}} = \frac{\tilde{\alpha} e E_0}{\hbar \omega_0^2} \cos \vartheta. \quad (47)$$

IV. DISCUSSION

The RING mechanism requires the ability to trace a loop in the qubit control parameter space and strong driving fields with respect to the Larmor frequency, see Fig. 1(c-d). These two key ingredients are achievable in several current quantum hardware platforms. Here, we discuss three of those platforms.

In nitrogen-vacancy center spin qubits, this loop can be realized by applying circularly polarized microwave drives to generate a rotating magnetic field, which has been already demonstrated [23, 24]. The circular polarization of the driving field is also beneficial due to selection rules: the circularly polarized light only drives one of the transitions between the $m = 0$ and $m = \pm 1$ spin-1 states. Moreover, strong driving amplitudes were also already used to perform coherent control of this platform [67].

Semiconductor spin qubits, particularly those with strong spin-orbit interaction such as hole-spin qubits in germanium [15, 16, 39, 68], offer another promising platform. Here, rotating effective fields can be generated electrically using multiple gate electrodes, which was already demonstrated in the context of bichromatic driving in Ref. [69]. Moreover, due to the fact that the effective driving amplitude of the qubit is proportional to the drive frequency, see Eq. (42), strong effective drive is feasible with moderate electric fields in the $\omega_L \ll \omega_d$ regime. The RING drive offers fast manipulation of qubits with low Larmor frequency, a setting which promises long qubit coherence times [39, 68]. For example, with the parameter values: $\alpha = 6500 \frac{\text{m}}{\text{s}}$, $E_0 = 2.5 \frac{\text{V}}{\text{mm}}$, $\omega_0/2\pi = 140 \text{ GHz}$ and $\vartheta = \pi/4$, one gets Rabi frequency, calculated from Eq. (42) substituting $\omega_L/2\pi = \omega_d/2\pi = 15 \text{ MHz}$ and multiplying it with $\sin \vartheta$, equals to $\Omega_R/2\pi \approx 0.45 \text{ MHz}$. While, the same parameters, with higher frequency drive $\omega_d/2\pi \approx 10.4 \text{ GHz}$ results in RING with Rabi frequency $\Omega_R/2\pi = \omega_L \tan \vartheta/2\pi = 15 \text{ MHz}$. Note that the circular resonant drive induces perfect Rabi oscillation, while in the case of RING Bloch–Siegert oscillation emerges with amplitude $A_{\text{BS}} \approx 0.023$, see Eq. (47).

Superconducting fluxonium qubits also provide a viable platform for RING. While the strong drive of flux qubits were demonstrated years ago [70], a recent work has shown how to simultaneously drive the qubit through both flux and gate voltage, thereby realizing a loop in the qubit’s parameter space [71]. This dual-drive capability directly enables the geometric control required for RING.

We also mention potential challenges for quantum logical gates relying on the RING mechanism. Avoiding adiabatic switching requires sub-nanosecond resolution, which was demonstrated already [39, 72]; and strong driving can induce Bloch–Siegert oscillations that reduce fidelity unless parameters are carefully tuned. One successful mitigation strategy against Bloch–Siegert oscillations is the use of *commensurate pulses*, where the Rabi frequency is made an integer multiple of the drive frequency. This method has been demonstrated in recent superconducting qubit experiments [71].

We further emphasize that the RING mechanism highlights several conceptually and practically significant aspects. First, it constitutes a demonstration of non-Abelian phases in the presence of a finite magnetic field, which is of fundamental interest and represents a stepping stone toward holonomic quantum computation. Second, because full Rabi oscillations are achieved under far-detuned driving, the scheme naturally enables the use of high-pass filtering, offering a route to suppress low-frequency and resonant noise. Finally, the mechanism does not rely on coherent energy exchange between the drive and the qubit, in contrast to conventional resonant control protocols.

V. CONCLUSIONS

We have explored an alternative route to coherent qubit control that does not rely on resonant energy exchange. Instead, complete Rabi oscillations arise from a geometric mechanism, activated when non-commuting drives trace a finite-area loop in control parameter space. With such ingredients, an effective coupling between qubit states emerges from the interference of off-resonant, virtual energy exchange processes. Using Floquet theory and numerical simulations, we established the conditions under which this nonresonant geometric drive (RING) produces complete Rabi oscillation in a two-level system. We further demonstrated that the effect can be realized using electric control in spin-orbit coupled quantum dots, leveraging established techniques in qubit manipulation. The required ingredients; strong, elliptical drive; are accessible in several current experimental platforms, suggesting that this geometric approach to quantum control may be experimentally testable in the near term.

ACKNOWLEDGMENTS

The authors thank G. Széchenyi, Z. György and Bence Hetényi for useful discussions. This research was supported by the Ministry of Culture and Innovation (KIM)

and the National Research, Development and Innovation Office (NKFIH) within the Quantum Information National Laboratory of Hungary (Grant No. 2022-2.1.1-NL-2022-00004), by the HUN-REN Hungarian Research Network through the HUN-REN-BME-BCE Quantum Technology Research Group, and by the European Union within the Horizon Europe research and innovation programme via the ONCHIPS project under grant agreement No 101080022. The project supported by the Doctoral Excellence Fellowship Programme (DCEP) is funded by the National Research Development and Innovation Fund of the KIM and the Budapest University of Technology and Economics, under a grant agreement with the NKFIH.

CODE AVAILABILITY

The code used to generate numerical results in this study has been made available at [66].

Appendix A: Numerical methods

The numerical solutions shown in Fig. 1(b-c) and Fig. 3(b-c) are implemented in python. The time-dependent Schrödinger equation is always solved via the discretization of time. The numerical time-evolution operator reads as

$$U(t) = \prod_{k=0}^{N-1} e^{-\frac{i}{\hbar} H(kdt)dt}. \quad (\text{A1})$$

To obtain the excited state probability we just used Born’s rule:

$$p_e(t) = |\langle \uparrow | U(t) | \downarrow \rangle|^2. \quad (\text{A2})$$

To obtain Fig. 1(b), we used $N = 50000$ steps. For Fig. 3(b), we have discretized the Hamiltonian in Eq. (21) in space on a 75×75 grid, with $a = 5.55$ nm discretization length. The dynamics were solved again by using Eq. (A1), but at each timestep, we have truncated the Hamiltonian, and only calculated the 6 smallest eigenvalue-eigenvector pair to construct the time-evolution operator. The duration of a timestep was $dt = 1/260 \cdot 2\pi/\omega_d$. To generate each point of Fig. 1(c) and Fig. 3(c), we have evaluated the numerical time-evolution operator in Eq. (A1) with the Hamiltonian defined in Eq. (1). For Fig. 3(c) we have used the parameters of the effective model defined in Eqs. (7). Both the Larmor and driving frequency axes has 400 points. The duration of a timestep was $dt = 1/500 \cdot 2\pi/\omega_d$, and the simulations were $T_{\max} = 1000 \cdot 2\pi/\omega_d$ long.

[1] M. Kjaergaard, M. E. Schwartz, J. Braumüller, P. Krantz, J. I.-J. Wang, S. Gustavsson, and W. D.

Oliver, Superconducting qubits: Current state of play,

- Ann. Rev. Condens. Matter Phys.* **11**, 369 (2020).
- [2] Y. Nakamura, Y. A. Pashkin, and J. S. Tsai, Coherent control of macroscopic quantum states in a single-Cooper-pair box, *Nature* **398**, 786 (1999).
- [3] D. Vion, A. Aassime, A. Cottet, P. Joyez, H. Pothier, C. Urbina, D. Esteve, and M. H. Devoret, Manipulating the quantum state of an electrical circuit, *Science* **296**, 886 (2002).
- [4] I. Chiorescu, Y. Nakamura, C. M. Harmans, and J. Mooij, Coherent quantum dynamics of a superconducting flux qubit, *Science* **299**, 1869 (2003).
- [5] A. Wallraff, D. I. Schuster, A. Blais, L. Frunzio, R.-S. Huang, J. Majer, S. Kumar, S. M. Girvin, and R. J. Schoelkopf, Strong coupling of a single photon to a superconducting qubit using circuit quantum electrodynamics, *Nature* **431**, 162 (2004).
- [6] V. E. Manucharyan, J. Koch, L. I. Glazman, and M. H. Devoret, Fluxonium: Single Cooper-pair circuit free of charge offsets, *Science* **326**, 113 (2009).
- [7] T. Harty, D. Allcock, C. Ballance, L. Guidoni, H. Janacek, N. Linke, D. Stacey, and D. Lucas, High-fidelity preparation, gates, memory, and readout of a trapped-ion quantum bit, *Phys. Rev. Lett.* **113**, 220501 (2014).
- [8] C. Ballance, T. Harty, N. Linke, M. Sepiol, and D. Lucas, High-fidelity quantum logic gates using trapped-ion hyperfine qubits, *Phys. Rev. Lett.* **117**, 060504 (2016).
- [9] G. Burkard, T. D. Ladd, A. Pan, J. M. Nichol, and J. R. Petta, Semiconductor spin qubits, *Rev. Mod. Phys.* **95**, 025003 (2023).
- [10] F. H. Koppens, C. Buizert, K. J. Tielrooij, I. T. Vink, K. C. Nowack, T. Meunier, L. P. Kouwenhoven, and L. M. Vandersypen, Driven coherent oscillations of a single electron spin in a quantum dot, *Nature* **442**, 766 (2006).
- [11] K. C. Nowack, F. H. L. Koppens, Y. V. Nazarov, and L. M. K. Vandersypen, Coherent control of a single electron spin with electric fields, *Science* **318**, 1430 (2007).
- [12] J. J. Pla, K. Y. Tan, J. P. Dehollain, W. H. Lim, J. J. L. Morton, D. N. Jamieson, A. S. Dzurak, and A. Morello, A single-atom electron spin qubit in silicon, *Nature* **489**, 541 (2012).
- [13] M. Veldhorst, J. C. C. Hwang, C. H. Yang, A. W. Leenstra, B. de Ronde, J. P. Dehollain, J. T. Muhonen, F. E. Hudson, K. M. Itoh, A. Morello, and A. S. Dzurak, An addressable quantum dot qubit with fault-tolerant control-fidelity, *Nat. Nanotechnol.* **9**, 981 (2014).
- [14] A. Crippa, R. Maurand, L. Bourdet, D. Kotekar-Patil, A. Amisse, X. Jehl, M. Sanquer, R. Laviéville, H. Bouslavskyi, L. Hutin, S. Barraud, M. Vinet, Y. M. Niquet, and S. De Franceschi, Electrical spin driving by g-matrix modulation in spin-orbit qubits, *Phys. Rev. Lett.* **120**, 137702 (2018).
- [15] F. N. M. Froning, L. C. Camenzind, O. A. H. van der Molen, A. Li, E. P. A. M. Bakkers, D. M. Zumbühl, and F. R. Braakman, Ultrafast hole spin qubit with gate-tunable spin-orbit switch functionality, *Nat. Nanotechnol.* **16**, 308 (2021).
- [16] N. W. Hendrickx, W. I. L. Lawrie, M. Russ, F. van Riggelen, S. L. de Snoo, R. N. Schouten, A. Sammak, G. Scappucci, and M. Veldhorst, A four-qubit germanium quantum processor, *Nature* **591**, 580 (2021).
- [17] S. G. J. Philips, M. T. Mądzik, S. V. Amitonov, S. L. de Snoo, M. Russ, N. Kalhor, C. Volk, W. I. L. Lawrie, D. Brousse, L. Tryputen, B. P. Wuetz, A. Sammak, M. Veldhorst, G. Scappucci, and L. M. K. Vandersypen, Universal control of a six-qubit quantum processor in silicon, *Nature* **609**, 919 (2022).
- [18] N. Wang, S.-M. Wang, R.-Z. Zhang, J.-M. Kang, W.-L. Lu, H.-O. Li, G. Cao, B.-C. Wang, and G.-P. Guo, Pursuing high-fidelity control of spin qubits in natural Si/SiGe quantum dot, *Appl. Phys. Lett.* **125**, 204002 (2024).
- [19] J. J. Pla, K. Y. Tan, J. P. Dehollain, W. H. Lim, J. J. L. Morton, F. A. Zwanenburg, D. N. Jamieson, A. S. Dzurak, and A. Morello, High-fidelity readout and control of a nuclear spin qubit in silicon, *Nature* **496**, 334 (2013).
- [20] G. C. Tettamanzi, S. J. Hile, M. G. House, M. Fuechsel, S. Rogge, and M. Y. Simmons, Probing the quantum states of a single atom transistor at microwave frequencies, *ACS Nano* **11**, 2444 (2017).
- [21] S. J. Hile, L. Fricke, M. G. House, E. Peretz, C. Y. Chen, Y. Wang, M. Broome, S. K. Gorman, J. G. Keizer, R. Rahman, and M. Y. Simmons, Addressable electron spin resonance using donors and donor molecules in silicon, *Sci. Adv.* **4**, eaaq1459 (2018).
- [22] M. Koch, J. G. Keizer, P. Pakkiam, D. Keith, M. G. House, E. Peretz, and M. Y. Simmons, Spin read-out in atomic qubits in an all-epitaxial three-dimensional transistor, *Nat. Nanotechnol.* **14**, 137 (2019).
- [23] T. P. M. Alegre, C. Santori, G. Medeiros-Ribeiro, and R. G. Beausoleil, Polarization-selective excitation of nitrogen vacancy centers in diamond, *Phys. Rev. B* **76**, 165205 (2007).
- [24] P. London, P. Balasubramanian, B. Naydenov, L. P. McGuinness, and F. Jelezko, Strong driving of a single spin using arbitrarily polarized fields, *Phys. Rev. A* **90**, 012302 (2014).
- [25] D. Schrader, I. Dotzenko, M. Khudaverdyan, Y. Miroshnychenko, A. Rauschenbeutel, and D. Meschede, Neutral atom quantum register, *Phys. Rev. Lett.* **93**, 150501 (2004).
- [26] Y. Wang, X. Zhang, T. A. Corcovilos, A. Kumar, and D. S. Weiss, Coherent addressing of individual neutral atoms in a 3D optical lattice, *Phys. Rev. Lett.* **115**, 043003 (2015).
- [27] T. Xia, M. Lichtman, K. Maller, A. W. Carr, M. J. Piotrowicz, L. Isenhower, and M. Saffman, Randomized benchmarking of single-qubit gates in a 2D array of neutral-atom qubits, *Phys. Rev. Lett.* **114**, 100503 (2015).
- [28] J. Levy, Universal quantum computation with spin-1/2 pairs and Heisenberg exchange, *Phys. Rev. Lett.* **89**, 147902 (2002).
- [29] J. R. Petta, A. C. Johnson, J. M. Taylor, E. A. Laird, A. Yacoby, M. D. Lukin, C. M. Marcus, M. P. Hanson, and A. C. Gossard, Coherent manipulation of coupled electron spins in semiconductor quantum dots, *Science* **309**, 2180 (2005).
- [30] B. M. Maune, M. G. Borselli, B. Huang, T. D. Ladd, P. W. Deelman, K. S. Holabird, A. A. Kiselev, I. Alvarado-Rodriguez, R. S. Ross, A. E. Schmitz, *et al.*, Coherent singlet-triplet oscillations in a silicon-based double quantum dot, *Nature* **481**, 344 (2012).
- [31] X. Wu, D. R. Ward, J. Prance, D. Kim, J. K. Gamble, R. Mohr, Z. Shi, D. Savage, M. Lagally, M. Friesen, *et al.*, Two-axis control of a singlet-triplet qubit with an integrated micromagnet, *Proc. Natl. Acad. Sci. U.S.A.* **111**, 11938 (2014).

- [32] D. Jirovec, A. Hofmann, A. Ballabio, P. M. Mutter, G. Tavani, M. Botifoll, A. Crippa, J. Kukucka, O. Sagi, F. Martins, *et al.*, A singlet-triplet hole spin qubit in planar Ge, *Nat. Mater.* **20**, 1106 (2021).
- [33] X. Zhang, E. Morozova, M. Rimbach-Russ, D. Jirovec, T.-K. Hsiao, P. C. Fariña, C.-A. Wang, S. D. Oosterhout, A. Sammak, G. Scappucci, *et al.*, Universal control of four singlet-triplet qubits, *Nat. Nanotechnol.* **20**, 209 (2025).
- [34] D. P. DiVincenzo, D. Bacon, J. Kempe, G. Burkard, and K. B. Whaley, Universal quantum computation with the exchange interaction, *Nature* **408**, 339 (2000).
- [35] J. Kempe, D. Bacon, D. A. Lidar, and K. B. Whaley, Theory of decoherence-free fault-tolerant universal quantum computation, *Phys. Rev. A* **63**, 042307 (2001).
- [36] A. J. Weinstein, M. D. Reed, A. M. Jones, R. W. Andrews, D. Barnes, J. Z. Blumoff, L. E. Euliss, K. Eng, B. H. Fong, S. D. Ha, *et al.*, Universal logic with encoded spin qubits in silicon, *Nature* **615**, 817 (2023).
- [37] S. Bosco and M. Rimbach-Russ, Exchange-only spin-orbit qubits in silicon and germanium, *Phys. Rev. Appl.* **25**, L021002 (2026).
- [38] F. K. Unseld, B. Undseth, E. Raymenants, Y. Matsumoto, S. L. de Snoo, S. Karwal, O. Pietx-Casas, A. S. Ivlev, M. Meyer, A. Sammak, *et al.*, Baseband control of single-electron silicon spin qubits in two dimensions, *Nat. Commun.* **16**, 5605 (2025).
- [39] C.-A. Wang, V. John, H. Tidjani, C. X. Yu, A. S. Ivlev, C. Déprez, F. van Riggelen-Doelman, B. D. Woods, N. W. Hendrickx, W. I. L. Lawrie, L. E. A. Stehouwer, S. D. Oosterhout, A. Sammak, M. Friesen, G. Scappucci, S. L. de Snoo, M. Rimbach-Russ, F. Borsoi, and M. Veldhorst, Operating semiconductor quantum processors with hopping spins, *Science* **385**, 447 (2024).
- [40] M. Rimbach-Russ, V. John, B. van Straaten, and S. Bosco, Gapless single-spin qubit, *Phys. Rev. Lett.* **135**, 197001 (2025).
- [41] G. Falci, R. Fazio, G. M. Palma, J. Siewert, and V. Vedral, Detection of geometric phases in superconducting nanocircuits, *Nature* **407**, 355 (2000).
- [42] A. A. Abdumalikov Jr., J. M. Fink, K. Juliusson, M. Pechal, S. Berger, A. Wallraff, and S. Filipp, Experimental realization of non-Abelian non-adiabatic geometric gates, *Nature* **496**, 482 (2013).
- [43] D. Leibfried, B. DeMarco, V. Meyer, D. Lucas, M. Barrett, J. Britton, W. M. Itano, B. Jelenković, C. Langer, T. Rosenband, *et al.*, Experimental demonstration of a robust, high-fidelity geometric two ion-qubit phase gate, *Nature* **422**, 412 (2003).
- [44] K. Toyoda, K. Uchida, A. Noguchi, S. Haze, and S. Urabe, Realization of holonomic single-qubit operations, *Phys. Rev. A* **87**, 052307 (2013).
- [45] S. Arroyo-Camejo, A. Lazariev, S. W. Hell, and G. Balasubramanian, Room temperature high-fidelity holonomic single-qubit gate on a solid-state spin, *Nat. Commun.* **5**, 4870 (2014).
- [46] C. Zu, W.-B. Wang, L. He, W.-G. Zhang, C.-Y. Dai, F. Wang, and L.-M. Duan, Experimental realization of universal geometric quantum gates with solid-state spins, *Nature* **514**, 72 (2014).
- [47] C. G. Yale, F. J. Heremans, B. B. Zhou, A. Auer, G. Burkard, and D. D. Awschalom, Optical manipulation of the berry phase in a solid-state spin qubit, *Nat. Photon.* **10**, 184 (2016).
- [48] Y. Sekiguchi, N. Niikura, R. Kuroiwa, H. Kano, and H. Kosaka, Optical holonomic single quantum gates with a geometric spin under a zero field, *Nat. Photon.* **11**, 309 (2017).
- [49] N. Ishida, T. Nakamura, T. Tanaka, S. Mishima, H. Kano, R. Kuroiwa, Y. Sekiguchi, and H. Kosaka, Universal holonomic single quantum gates over a geometric spin with phase-modulated polarized light, *Opt. Lett.* **43**, 2380 (2018).
- [50] B. B. Zhou, P. C. Jerger, V. O. Shkolnikov, F. J. Heremans, G. Burkard, and D. D. Awschalom, Holonomic quantum control by coherent optical excitation in diamond, *Phys. Rev. Lett.* **119**, 140503 (2017).
- [51] K. Nagata, K. Kuramitani, Y. Sekiguchi, and H. Kosaka, Universal holonomic quantum gates over geometric spin qubits with polarised microwaves, *Nat. Commun.* **9**, 3227 (2018).
- [52] Z.-P. Hong, B.-J. Liu, J.-Q. Cai, X.-D. Zhang, Y. Hu, Z. Wang, and Z.-Y. Xue, Implementing universal non-adiabatic holonomic quantum gates with transmons, *Phys. Rev. A* **97**, 022332 (2018).
- [53] V. N. Golovach, M. Borhani, and D. Loss, Holonomic quantum computation with electron spins in quantum dots, *Phys. Rev. A* **81**, 022315 (2010).
- [54] P. San-Jose, B. Scharfenberger, G. Schön, A. Shnirman, and G. Zarand, Geometric phases in semiconductor spin qubits: Manipulations and decoherence, *Phys. Rev. B* **77**, 045305 (2008).
- [55] B. Kolok and A. Pályi, Protocols to measure the non-Abelian Berry phase by pumping a spin qubit through a quantum-dot loop, *Phys. Rev. B* **109**, 045438 (2024).
- [56] J. H. Shirley, Solution of the Schrödinger equation with a Hamiltonian periodic in time, *Phys. Rev.* **138**, B979 (1965).
- [57] J. Romhányi, G. Burkard, and A. Pályi, Subharmonic transitions and Bloch-Siegert shift in electrically driven spin resonance, *Phys. Rev. B* **92**, 054422 (2015).
- [58] S. Bravyi, D. P. DiVincenzo, and D. Loss, Schrieffer-Wolff transformation for quantum many-body systems, *Ann. Phys.* **326**, 2793 (2011).
- [59] M. Bükov, L. D'Alessio, and A. Polkovnikov, Universal high-frequency behavior of periodically driven systems, *Adv. Phys.* **64**, 139 (2015).
- [60] R. Winkler, Appendix B: Quasi-degenerate perturbation theory, in *Spin-orbit coupling effects in two-dimensional electron and hole systems* (Springer Berlin, Heidelberg, Berlin, Heidelberg, 2003) pp. 201–205.
- [61] S. Rahav, I. Gilary, and S. Fishman, Effective Hamiltonians for periodically driven systems, *Phys. Rev. A* **68**, 013820 (2003).
- [62] T. Mikami, S. Kitamura, K. Yasuda, N. Tsuji, T. Oka, and H. Aoki, Brillouin-Wigner theory for high-frequency expansion in periodically driven systems: Application to Floquet topological insulators, *Phys. Rev. B* **93**, 144307 (2016).
- [63] F. Bloch and A. Siegert, Magnetic resonance for nonrotating fields, *Phys. Rev.* **57**, 522 (1940).
- [64] F. Wilczek and A. Zee, Appearance of gauge structure in simple dynamical systems, *Phys. Rev. Lett.* **52**, 2111 (1984).
- [65] A. Bohm, A. Mostafazadeh, H. Koizumi, Q. Niu, and J. Zwanziger, Mathematical structure of the geometric phase II: the non-Abelian phase, in *The geometric phase in quantum systems: foundations, mathematical*

- concepts, and applications in molecular and condensed matter physics* (Springer Berlin, Heidelberg, Berlin, Heidelberg, 2003) pp. 129–145.
- [66] B. Kolok, [Code to generate figures for "RING: Rabi oscillations induced by nonresonant geometric drive"](#), Zenodo (2026).
- [67] G. Fuchs, V. Dobrovitski, D. Toyli, F. Heremans, C. Weis, T. Schenkel, and D. Awschalom, Excited-state spin coherence of a single nitrogen–vacancy centre in diamond, [Nat. Phys. 6, 668 \(2010\)](#).
- [68] N. W. Hendrickx, L. Massai, M. Mergenthaler, F. J. Schupp, S. Paredes, S. W. Bedell, G. Salis, and A. Fuhrer, Sweet-spot operation of a germanium hole spin qubit with highly anisotropic noise sensitivity, [Nat. Mater. 23, 920 \(2024\)](#).
- [69] V. John, F. Borsoi, Z. György, C.-A. Wang, G. Széchenyi, F. van Riggelen-Doelman, W. I. L. Lawrie, N. W. Hendrickx, A. Sammak, G. Scappucci, A. Pályi, and M. Veldhorst, Bichromatic Rabi control of semiconductor qubits, [Phys. Rev. Lett. 132, 067001 \(2024\)](#).
- [70] F. Yoshihara, Y. Nakamura, F. Yan, S. Gustavsson, J. Bylander, W. D. Oliver, and J.-S. Tsai, Flux qubit noise spectroscopy using Rabi oscillations under strong driving conditions, [Phys. Rev. B 89, 020503 \(2014\)](#).
- [71] D. A. Rower, L. Ding, H. Zhang, M. Hays, J. An, P. M. Harrington, I. T. Rosen, J. M. Gertler, T. M. Hazard, B. M. Niedzielski, M. E. Schwartz, S. Gustavsson, K. Serniak, J. A. Grover, and W. D. Oliver, Suppressing counter-rotating errors for fast single-qubit gates with fluxonium, [PRX Quantum 5, 040342 \(2024\)](#).
- [72] F. van Riggelen-Doelman, C.-A. Wang, S. L. de Snoo, W. I. Lawrie, N. W. Hendrickx, M. Rimbach-Russ, A. Sammak, G. Scappucci, C. Déprez, and M. Veldhorst, Coherent spin qubit shuttling through germanium quantum dots, [Nat. Commun. 15, 5716 \(2024\)](#).